



## Elastic properties of $\alpha$ - and $\beta$ -tantalum thin films

G. Abadias, J.J. Colin, D. Tingaud, Ph. Djemia, Laurent Belliard, C. Tromas

### ► To cite this version:

G. Abadias, J.J. Colin, D. Tingaud, Ph. Djemia, Laurent Belliard, et al.. Elastic properties of  $\alpha$ - and  $\beta$ -tantalum thin films. Thin Solid Films, 2019, 688, pp.137403. 10.1016/j.tsf.2019.06.053 . hal-02457454

**HAL Id: hal-02457454**

**<https://hal.science/hal-02457454>**

Submitted on 21 Dec 2021

**HAL** is a multi-disciplinary open access archive for the deposit and dissemination of scientific research documents, whether they are published or not. The documents may come from teaching and research institutions in France or abroad, or from public or private research centers.

L'archive ouverte pluridisciplinaire **HAL**, est destinée au dépôt et à la diffusion de documents scientifiques de niveau recherche, publiés ou non, émanant des établissements d'enseignement et de recherche français ou étrangers, des laboratoires publics ou privés.



Distributed under a Creative Commons Attribution - NonCommercial 4.0 International License

## Elastic properties of $\alpha$ - and $\beta$ -tantalum thin films

G. Abadias<sup>1</sup>, J.J. Colin<sup>1</sup>, D. Tingaud<sup>2</sup>, Ph. Djemia<sup>2</sup>, L. Belliard<sup>3</sup>, C. Tomas<sup>1</sup>

1. Institut Pprime, Département Physique et Mécanique des Matériaux, UPR 3346, CNRS-Université de Poitiers-ENSMA, SP2MI, Téléport 2, F86962, Futuroscope-Chasseneuil, France
2. Laboratoire des Sciences des Procédés et des Matériaux, LSPM-CNRS 3407, Sorbonne Paris Cité, 99 Avenue J.B. Clément, 93430 Villetaneuse, France
3. Sorbonne Université, UPMC Université Paris 06, INSP UMR CNRS 7588, 4 Place Jussieu, 75005 Paris, France

### Abstract

We comparatively study the elastic properties of the two existing polytypes of tantalum,  $\alpha$ -Ta (ground state bcc structure) and  $\beta$ -Ta (metastable tetragonal structure), using density functional theory (DFT) calculations and thin film growth experiments. The lattice parameter and the single-crystal elastic constants  $c_{ij}$  for the two allotropic structures were computed using pseudo-potentials with generalized gradient approximation. Sound velocity measurements on single-phase, highly-textured (001)  $\beta$ -Ta and (110)  $\alpha$ -Ta films deposited by magnetron sputtering were carried out using picosecond laser ultrasonic and Brillouin light scattering techniques, while hardness  $H$  and Young's modulus  $E$  were measured using nanoindentation. We found that the  $\beta$ -Ta phase is significantly harder ( $H \sim 18.0$  GPa) than  $\alpha$ -Ta ( $H \sim 10.3$  GPa), while their elastic stiffness properties and Cauchy pressure  $p$  are similar,  $C_{33} \sim 285$ -310 GPa,  $E \sim 188$  GPa,  $p \sim 70$ -80 GPa, and agree well with the computed values. However, the out-of-plane shear modulus  $G$  of the  $\beta$ -Ta film is softer by 28% with respect to that of  $\alpha$ -Ta film and DFT values (50 vs. 69 GPa). The present findings reveal that, contrarily to common claims, the  $\beta$ -Ta phase is not at all brittle but

elastically and plastically deforms in a compliant way. Its toughness and elastic strain to failure ability is further comprehended from low  $G/B$  (0.205) and high  $H/E$  ( $\approx 0.1$ ) ratios and the absence of radial cracks around indents, which suggests that  $\beta$ -Ta is also a suitable phase for use as wear-resistant coating in biomedical applications.

## I. Introduction

Tantalum (Ta) is a refractory metal that combines very attractive properties, such as high-temperature stability ( $T_m \sim 3000^\circ\text{C}$ ), high density ( $16.6 \text{ g.cm}^{-3}$ ), good conductivity, corrosion resistance and biocompatibility. It also offers robust mechanical properties, such as high hardness, low brittle-to-ductile temperature ( $<20 \text{ K}$ ) and wear resistance. For these reasons, Ta and its alloys, as well as Ta thin films, have seen use in diverse technological areas such as, electronics [1,2], ballistic rockets and spacecrafts [1], protective coatings [3] and more recently in orthopedic implants and biomedical applications [4–9].

In thin film form, it is well known that two different crystallographic phases of Ta can be synthesized: the thermodynamically stable  $\alpha$ -Ta with a body-centered-cubic (bcc) structure and a metastable tetragonal structure (referred as  $\beta$ -Ta), although there exist some reports about the stabilization of a third phase with face-centered cubic (fcc) structure, due to the presence of impurities [10–12]. The  $\alpha$ -Ta phase is usually difficult to obtain by sputter-deposition without the assistance of substrate heating [3,13–15], post-annealing treatment [16–18] or the use of specific seed layers [15,19–21]. Numerous works have been devoted over the last years in efforts to relate the influence of sputter-deposition conditions on phase selection, and elucidate the underlying mechanisms which control the nucleation process [22–29]. Examination of the literature data reveals disparate and confusing results [15,29], essentially because in many reports the produced tantalum films contained a mixture of both  $\alpha$ - and  $\beta$ -phases, and were operated under different vacuum level and/or impurity control conditions. We have recently shown that the preferential nucleation of  $\beta$ -Ta with (002) orientation is driven by a lower activation barrier, as a result of interface energy minimization [15], and that it does not

necessarily require the presence of oxygen species at the substrate surface, which does not support the scenario proposed afterwards by Ellis *et al.* [29].

The  $\alpha$ -Ta and  $\beta$ -Ta phases have very different electrical properties: room-temperature resistivities of pure  $\beta$ -Ta films are in the 150-200  $\mu\Omega\cdot\text{cm}$  range, which is typically one order of magnitude higher than those of  $\alpha$ -Ta films ( $\rho \sim 20\text{-}30 \mu\Omega\cdot\text{cm}$ ), the resistivity of bulk single-crystal  $\alpha$ -Ta being 13.6  $\mu\Omega\cdot\text{cm}$  [2,15,21,22,30,31].  $\beta$ -Ta films additionally exhibit a low, or even negative, temperature coefficient of resistivity [30,32] and are predominantly used as thin film resistors.

The mechanical properties of these two allotropic phases appear also quite distinct: compared to the relatively ductile  $\alpha$ -Ta phase,  $\beta$ -Ta is said to be harder and more brittle. The higher degree of brittleness of  $\beta$ -Ta thin films would make them unsuitable for applications as orthopedic implants, where fracture toughness and elastic compliance with biomedical Ti- or Co-based alloys are essential requisites. This claim is essentially based on nanoindentation studies. Hardness values reported by Zhang *et al.* [33,34] and Shiri *et al.* [4] confirm the higher hardness ( $\sim 20\%$ ) of magnetron-sputtered  $\beta$ -Ta films compared to  $\alpha$ -Ta films: 15 GPa vs. 12 GPa [33,34] and  $19 \pm 0.7$  GPa vs.  $15 \pm 0.4$  GPa [4], respectively, while the elastic modulus is found to be only slightly larger (less than 10%) for  $\beta$ -Ta in comparison with that of  $\alpha$ -Ta, being 194 GPa vs. 178 GPa [34], and  $229 \pm 14$  GPa vs.  $211 \pm 8$  GPa [4], respectively. However, from an independent work, Knepper and Baker [18] reported more compliant properties of  $\beta$ -Ta films compared to  $\alpha$ -Ta ones from the analysis of their thermoelastic behaviors. The biaxial elastic modulus of  $\beta$ -Ta was found to be more than 50% lower than that of  $\alpha$ -Ta ( $175 \pm 20$  GPa vs.  $270 \pm 30$  GPa), indicating a significantly lower stiffness of the  $\beta$  phase. This conflicts with the

experimental work of Frank *et al.* [35] on the cohesive properties of  $\alpha$ -Ta and  $\beta$ -Ta coatings derived from uniaxial tensile tests on polyimide substrates.

To disentangle these findings, a more accurate assessment of the mechanical properties and ductility trends of  $\alpha$ -Ta and  $\beta$ -Ta polycrystalline films requires the independent knowledge of their effective  $C_{ij}$  elastic constants. If computed and experimentally measured  $C_{ij}$  values exist for the  $\alpha$ -Ta phase [36–39], on the other hand, a corresponding database is not yet available in the literature for the  $\beta$ -Ta phase. In the present work, we contribute to fill this gap by investigating the elastic properties of single-phase  $\alpha$ -Ta and  $\beta$ -Ta thin films, based on first-principles calculations and direct measurements of sound velocities. By comparing the computed single-crystal stiffness constants  $c_{ij}$  and the effective elastic constants  $C_{ij}$  of magnetron-sputtered Ta films obtained by coupling picosecond laser ultrasonics (PLU) and Brillouin light spectroscopy (BLS), the influence of film microstructural attributes (thickness, grain size, texture) on *polycrystalline* elastic moduli (Young's modulus  $E$ , shear modulus  $G$  and bulk modulus  $B$ ) is addressed. Our results show that  $\beta$ -Ta films exhibit a lower  $G/B$  ratio and Debye temperature  $\theta_D$  than  $\alpha$ -Ta films, suggesting their more ductile character.

## II. Methodology

### II.1. Computational procedure

The static (0 K) atomic-scale calculations were carried out with the Vienna ab initio simulation package (VASP) [40], which implements projector augmented wave pseudo-potentials (PP) [41] and the Perdew-Burke-Ernzerhof [42] exchange-correlation functional in the generalized gradient approximation (GGA). A cut-off energy of 340 eV and a  $k$ -point sampling of 15x15x15 and 4x4x8 for  $\alpha$ -Ta- and  $\beta$ -Ta, respectively, are sufficient to ensure an energy

convergence below 0.5 meV/atom and a convergence threshold of  $10^7$  Pa was taken for the pressure.

The  $\alpha$  tantalum has a bcc structure (space group  $Im\bar{3}m$ ), while the  $\beta$  tantalum is a tetragonal cell of  $P\bar{4}2_1m$  structure which contains 30 atoms per unit cell, as described by Arakcheeva *et al.* [43], see [Figure 1](#). The Wyckoff positions of Ta atoms in the tetragonal cell are given in [Table 1](#). Single-lattice supercells were fully relaxed with respect to volume and cell-internal parameters. Around the equilibrium state the supercells were deformed through appropriate stress tensors, see for example Refs. [44,45] for the case of the tetragonal phase. Energy variations according to the strain were fitted by a quadratic function or by the Murnaghan's equation of state[46] which reduces the fitting error (which remain below 1%) in the case of non-isochore lattice deformation to extract the different elastic constants.

## II.2. Experimental details

### II.2.1. Thin film growth and characterization

Ta films were sputter-deposited at room temperature under Ar plasma discharge in a high vacuum (base pressure  $8 \times 10^{-6}$  Pa) chamber designed by Alliance Concept and equipped with three confocal, water-cooled, 3" planar magnetron sources [47,48]. Prior to deposition, the Ta target (99.99% purity) was sputter-cleaned during 5 min to remove surface contaminant. The cathode was electrically connected to an MDX 1500 Advanced Energy power supply, that was operated at constant power (80 W), in DC mode, and using a balanced magnetron configuration. The Ar working pressure was kept constant at 0.24 Pa, resulting in a discharge voltage of  $\sim 335$  V. The target-to-substrate distance was 18 cm, and the substrates were grounded.

Single-phase  $\alpha$ -Ta and  $\beta$ -Ta films were grown on crystalline molybdenum (c-Mo) and amorphous silicon (a-Si) seed layer, respectively. These underlayers, with thickness  $\sim 10$  nm, were sputter-deposited in the same chamber on (001) Si wafer covered with native oxide. More details on the deposition process can be found elsewhere [15]. Two different deposition times (1250 and 3750 s) were selected to produce Ta films with nominal thicknesses of  $\sim 100$  and  $\sim 300$  nm.

The phase identification, crystal structure and surface morphology were characterized by X-ray Diffraction (XRD) and atomic force microscopy (AFM), respectively.  $\theta$ - $2\theta$  scans were acquired in Bragg-Brentano geometry using a Cu X-ray tube operating at  $\lambda = 0.15418$  nm. AFM observations have been performed in tapping mode using a D3100 microscope from Bruker (Santa Barbara, CA) and the images processed with the WSxM software [49].

The elastic properties were assessed by coupling complementary BLS and PLU techniques [50,51], as well as nanoindentation tests. The nanoindentation tests have been performed on the thicker Ta films with a U-NHT nanoindenter from Anton Paar Tritec (Peseaux, Switzerland), equipped with a diamond Berkovich indenter. The shape of the indenter has been carefully calibrated, for penetration depths as low as 15 nm, by indenting a reference material (fused silica) of known Young's modulus. The Hardness and the elastic modulus have been determined by analyzing the elastic unloading curves using the effective indenter method [52,53]. BLS and PLU techniques are briefly described hereafter.

### II.2.2. *Measurement of sound velocities*

In the present case of Ta films, a standard PLU approach [54–57] is convenient to extract the longitudinal sound velocity,  $V_L$ . The PLU technique uses femtosecond laser pulses to



generate and detect acoustic waves, with typical frequency range from 100 GHz up to 1 THz. In brief, this technique relies on the absorption of a femtosecond laser pulse (the pump beam) at the sample surface, generating acoustic waves which propagate through the system along the surface normal. After being reflected at the substrate/film interface the acoustic wave is probed at the free surface by a time-delayed laser pulse (the probe beam). In opaque systems, and for the case of a monolithic thin film on a substrate, periodic echoes are typically observed in the transient reflectivity profile. The longitudinal velocity is simply defined by  $V_L = 2h / \Delta t$ , where  $\Delta t$  is the time delay between two consecutive echoes, measured with an accuracy better than 1 ps, and  $h$  the film thickness. From  $V_L$ , the  $C_{33}$  effective elastic constant, along the normal of the film surface, can be derived straightforwardly using the relationship  $C_{33} = \rho V_L^2$ , where  $\rho$  is the film mass density. In our experimental set-up, we use a mode-locked Ti:Sapphire laser source, operating at 800 nm with a repetition rate around 79.3 MHz. The pump beam is modulated at 1.8 MHz to improve the signal-to-noise ratio. More details, as well as a schematic of the experimental set-up, can be found in Refs. [50,51].

The transverse sound velocity  $V_T$  was measured from BLS experiments, which use a monochromatic light beam to probe the thermally excited acoustic waves naturally present in the investigated medium [58]. Because of the wave vector conservation rule in the phonon–photon interaction, the wavelength of the revealed elastic waves is of the same order of magnitude as that of light and then is much larger than the interatomic distances, so that the material can be described as a continuous effective-medium. Here, we used the backscattering interaction geometry, so that the modulus value of the wave vector ( $\mathbf{Q}$ ) of the probed surface acoustic waves travelling parallel to the film-plane is fixed experimentally to the value  $Q = 2k_i \sin(\theta)$ , where  $k_i$  denotes the incident optical wave vector in air and  $\theta$  the incidence angle of the

light with respect to surface normal. The acoustical wavelength ( $\Lambda$ ) is simply defined as  $\Lambda = 2\pi/Q$  and the velocity ( $V$ ) of a surface acoustic wave is obtained from the frequency measurements  $f$  thanks to the relation  $V = f * \Lambda$ . The BLS spectra were obtained at room temperature in air, with typical acquisition times of 2 h, for three different angles  $\theta = 50, 60$  and  $70^\circ$ . The light source was a YAG solid laser with single mode of 532 nm. Typically, 300 mW of a naturally p-polarized light was focused on the surface of the sample and the backscattered light was analyzed by means of a Sandercock-type 3 + 3 pass tandem Fabry–Perot interferometer.

For nearly opaque layers, such as the present Ta films with metallic character, the scattering mechanism is restricted to the scattering of light by the dynamical corrugation of the free surface by acoustic waves travelling parallel to the film plane [59]. Thus, we can only observe the surface acoustic waves with a sagittal polarization (first component along the  $Q$  direction and the second is vertical). For films with thicknesses around the acoustic wavelength ( $\sim 300$  nm) and deposited on a substrate with higher acoustic phase velocity (“slow” film on “fast” substrate), the surface acoustic waves with a sagittal polarization are: the Rayleigh wave (R) and the so-called Sezawa guided waves ( $S_1$ – $S_n$ ) [59] at higher frequencies. The frequency (velocity) and number of these  $S_i$  surface modes are dependent on both the thickness and the elastic constants of the film and of the substrate, whereas the velocity of the Rayleigh surface wave,  $V_R$ , is mainly dependent on the transverse velocity  $V_T = (C_{44}/\rho)^{1/2}$  [60] through the relation  $V_R = \beta V_T$ , where  $\beta \sim 0.92$  is a slightly varying function of the whole elastic constants of the film.

If the longitudinal and transverse sound velocities  $V_L$  and  $V_T$  can be readily assessed from PLU and BLS measurements, the determination of the effective  $C_{33}$  and  $C_{44}$  elastic constants requires accurate knowledge of the film thickness  $h$  and mass density  $\rho$ . These two quantities

were extracted from X-ray reflectometry (XRR) on the thin film series, by fitting an optical model based on Parratt's formalism [61] to the experimental data. XRR scans were acquired on a Seifert XRD3000 diffractometer equipped with a line focus Cu source, a primary channel cut monochromator selecting the Cu  $K_{\alpha 1}$  line with a low divergence, and a scintillation detector defined with a 0.07 mm slit.

### III. Results

#### III.1. Structural parameters

[Table 2](#) collects the computed lattice parameters of  $\alpha$ -Ta and  $\beta$ -Ta using the present DFT calculations. Good agreements are found for both phases when compared to available literature data for  $\alpha$ -Ta [37–39] and  $\beta$ -Ta [43]. The calculated atomic volume  $V_a$  (18.2 and 18.7 Å<sup>3</sup> for  $\alpha$ -Ta and  $\beta$ -Ta, respectively,) also compares within 5% with the one derived from the mass density measured by XRR, see [Table 3](#). For  $\alpha$ -Ta, our DFT calculations also reproduce to within 1-5% the computed values by Söderling and Moriarty [37] ( $V_a=17.68$  Å<sup>3</sup>) based on full-potential linear muffin-tin orbitals (LMTO) method or by Strachan *et al.* [38] ( $V_a=18.33$  Å<sup>3</sup>) based on linear augmented plane wave (LAPW) method.

[Figure 2](#) shows the XRR scans of Ta thin films deposited on c-Mo (blue curve) and  $\alpha$ -Si (red curve) underlayers. The scans are very similar, in terms of critical angle, intensity decay of the specular reflectivity and periodicity of high-frequency intensity modulations (Kiessig's fringes), suggesting films with similar material properties. For the c-Mo/Ta film, one can notice the presence of a low-frequency intensity modulation (arising from the c-Mo buffer layer) that it is not observed for the  $\alpha$ -Si/Ta system due to similar densities between  $\alpha$ -Si buffer and Si

substrate. Measured XRR scans were fit to theoretical reflectivity curves calculated from the recursive theory of Parratt [61] using proprietary Analyze® software. Best-fit parameters yield similar film thickness (107 and 109 nm for these films) and mass density (17.1 and 16.6 g.cm<sup>-3</sup>), see Table 3, the film deposited on c-Mo being slightly rougher (1.8 vs. 1.4 nm). These results show that Ta films deposited under the present deposition conditions develop a very dense microstructure (the bulk mass density value for  $\alpha$ -Ta and  $\beta$ -Ta is 16.6 [36] and 16.3 g.cm<sup>-3</sup> [43], respectively) with smooth surface. The obtained mass density values are slightly higher by 2-3% compared to bulk values, which can be understood by the relatively high energy of the incoming particles (mean energy of 57 eV at 0.24 Pa, see ref. [15]), which contributes to densify the film but also to introduce point defects. These conditions result to the development of compressive stress (~1.5 GPa), as previously reported by Colin *et al.* [15]. For the thicker film series, Kiessig's fringes are not anymore observable, so the film thickness was estimated from the deposition time and the deposition rate  $R$  as obtained on the thin film series, with  $R=0.086 \pm 0.001$  nm/s. It is worth mentioning that both  $\alpha$ -Ta and  $\beta$ -Ta films are remarkably stable when stored at ambient air after more than four years, as no significant changes could be detected in their XRR.

Figure 3 shows the XRD patterns recorded on a large angular range for the Ta films deposited on  $\alpha$ -Si and c-Mo buffer layers. In both cases, films are single-phase and exhibit a high degree of preferred orientation (fiber-texture). Ta films growing on c-Mo develop a bcc structure and (110)-texture (Fig. 3b), while the metastable  $\beta$ -Ta phase obtained on  $\alpha$ -Si has a strong (002) texture (Fig. 3a). For  $\beta$ -Ta, odd reflections indexed as 001 and 003 were detected (see Fig. 3c), as also reported by Ellis *et al.* [29]. These are not compatible with centrosymmetric  $P4_2/mnm$  group and confirm a crystal structure belonging to the  $P\bar{4}2_1m$  space group, as reported by Arakcheeva *et al.* [43].

The lattice parameter of the  $\alpha$ -Ta film calculated from the 110 and 220 peak positions at  $2\theta=38.17^\circ$  and  $81.62^\circ$ , respectively, is  $a=0.333 \pm 0.001$  nm, which concurs with reported values of bulk  $\alpha$ -Ta (0.331 nm), as well as computed values reported in Table 2. The  $c$ -lattice parameter of  $\beta$ -Ta films is 0.532 nm, in excellent agreement with reference data (ICCD card n° 25-1280) and the present DFT calculations (see Table 2). The grain size was evaluated from the XRD line broadening using the Williamson-Hall method [62]. The size of coherent domains (along the growth direction) was found to be on the order of magnitude of the film thickness, pointing out to the development of columnar grains extending throughout the entire layer.

Cross-sectional scanning electron microscopy (SEM) observations (not shown) confirm the columnar morphology of the films. However, the surface morphology of the two films was notably distinct. As it can be seen from plan-view AFM and SEM images of Fig. 4, the surface of  $\beta$ -Ta film is extremely smooth with shallow mounds hardly discernable, while a needle-shaped faceted surface is observed for  $\alpha$ -Ta. The presence of such facets is typical for bcc metallic films with (110) texture and has been ascribed to the formation of nanoridge domains during growth [63]. Analysis of the AFM images confirms a higher surface roughness for  $\alpha$ -Ta (1.1 nm) compared to  $\beta$ -Ta (0.4 nm).

Additional transmission electron microscopy observations (not reported here) confirm the structural identification obtained by XRD, and the template effect of the  $c$ -Mo buffer layer in promoting by local epitaxy the growth of the  $\alpha$ -Ta phase [15].

The room-temperature electrical resistivity of the films was measured using a standard four-point probe technique (Van der Pauw geometry). Values, reported in Table 3, confirm the more resistive electrical character of  $\beta$ -Ta films ( $\sim 170 \mu\Omega\cdot\text{cm}$ ) compared to  $\alpha$ -Ta ones ( $21 \mu\Omega\cdot\text{cm}$ ).

### III.2. Single-crystal elastic constants

The static elastic constants calculated for the cubic  $\alpha$ -Ta structure are  $c_{11}=260$  GPa,  $c_{12}=157$  GPa and  $c_{44}=79$  GPa. They are in good agreement with prior *ab initio* calculations by Bercegeay *et al.* [39] using a similar approach, as well as by Strachan *et al.* [38] and Söderlind and Moriarty [37] based on all-electron methods (see [Table 2](#)), both with GGA scheme. They also agree within 2-10% with measured adiabatic  $c_{ij}$  values obtained from ultrasonic experiments on  $\alpha$ -Ta single-crystals [36,64]. The elastic properties of the  $P\bar{4}2_1m$  tetragonal  $\beta$ -Ta structure are completely described by six independent constants ( $c_{11}$ ,  $c_{12}$ ,  $c_{13}$ ,  $c_{33}$ ,  $c_{44}$ , and  $c_{66}$ ). The longitudinal elastic constant  $c_{11}$  or  $c_{33}$  is higher for  $\beta$ -Ta ( $\sim 300$  GPa) compared to that of  $\alpha$ -Ta (260 GPa), whereas the out-of-plane shear elastic constant  $c_{44}$  or  $c_{66}$  shows an opposite trend:  $c_{44}=69$  GPa for  $\beta$ -Ta and 79 GPa for  $\alpha$ -Ta. These  $c_{ij}$ 's will serve as initial input to estimate the effective elastic properties of our fiber-textured Ta films, using the self-consistent (SC) averaging method [65,66] presented in the next section.

### III.3. Effective elastic properties

Some results of PLU and BLS experiments are illustrated in [Figs. 5](#) and [6](#) for  $\alpha$ -Ta and  $\beta$ -Ta films belonging to the thicker film series. We can notice in [Fig. 5](#) that the time-resolved response associated to each echo exhibits a different shape between the  $\alpha$ -Ta and  $\beta$ -Ta phases. This feature is correlated to the optical index and photo-elastic coefficient of the material [57]. The different shape of the acoustic echoes traduces a different electronic structure, which is also reflected by distinct electrical resistivities, see [Table 3](#).

The values of  $V_L$ , deduced from the time of flight (TOF) of echoes, and  $V_T$ , extracted from a fit of BLS spectra (see Fig. 6), are reported in Table 3 together with the effective elastic constant  $C_{33}$  and  $C_{44}$ . Similar  $V_L$  values around 4 km/s are found for both phases, while  $V_T$  is 14% slower for  $\beta$ -Ta (1.7 km/s) compared to  $\alpha$ -Ta (2.0 km/s). We find the same trends for the effective elastic constants as for the single-crystal elastic constants: the longitudinal  $C_{33}$  constant is slightly higher for  $\beta$ -Ta (310 GPa) compared to the  $\alpha$ -Ta phase (285 GPa), whereas the shear elastic constant  $C_{44}$  is lower for  $\beta$ -Ta (50 GPa) compared to the  $\alpha$ -Ta phase (69 GPa). It is important to note that for the case of these highly textured (110)  $\alpha$ -Ta and (001)  $\beta$ -Ta films,  $C_{33}$  (measured in the sample frame) is equal to  $(c_{11}+c_{12}+2c_{44})/2$  and  $c_{33}$  (in the crystal frame), respectively. Thus, we can have a direct access to some single-crystal elastic constants  $c_{ij}$ 's, even for a polycrystalline material.

The experimental  $C_{33}$  and  $C_{44}$  values are compared to calculated SC average effective elastic constants  $\langle C_{33} \rangle$  and  $\langle C_{44} \rangle$  (see Table 4), using the single-crystal  $c_{ij}$  values of Table 2 and taking into account the (110) and (001) texture of the  $\alpha$ -Ta and  $\beta$ -Ta films, respectively. A very good agreement is obtained with experimental data, except for the out-of-plane shear modulus of  $\beta$ -Ta ( $\langle C_{44} \rangle = 68$  GPa) that is 30% over-estimated compared to the experimental value ( $C_{44} = 50$  GPa). This softening would be beneficial for lowering of  $G/B$  Pugh's ratio [67] and consequently, for improving the ductility, as it will be discussed in Sect. IV.

This apparent softening may be accounted for by the presence of point defects in the films (interstitials type) that are not considered in our DFT defect-free calculations. For example, working gas (Ar) atoms can be implanted in the growing film due to a large fraction of energetic ( $> 80$  eV) Ar atoms reflected from the target. The Ar content, measured by Rutherford

backscattering spectroscopy, reached typically 3 at.% in these Ta films [15]. The consequence on structural and elastic properties of such Ar incorporation has not been specifically studied. Nevertheless, the influence of C and N interstitials distribution on the elastic properties of  $\epsilon$ -Fe<sub>6</sub>C<sub>x</sub>N<sub>y</sub> hexagonal crystals has been theoretically investigated by first-principles calculations [68]. Variations of up to 30% were found for single-crystal elastic constants  $c_{11}$ ,  $c_{33}$  or  $c_{44}$ , as well as for polycrystalline elastic moduli ( $E$  and  $G$ ), depending on defect concentration and configuration. In our previous work on sputter-deposited Mo films, we observed a softening of the  $C_{44}$  (up to 30%) and  $C_{33}$  (up to 14%) constants compared to Mo bulk values [56]. A larger decrease was found for ion beam sputtered films ( $C_{44}$ = 98 GPa) than for magnetron sputtered films ( $C_{44}$ =115 GPa), as the former, more energetic, deposition condition induced more defects in the resulting film, also associated with a larger mass density.

### III.4 Nanoindentation results

Figure 7a displays the hardness and elastic modulus profiles determined by nanoindentation for different penetration depths in the  $\alpha$ -Ta and  $\beta$ -Ta samples. Each point corresponds to the average of ten independent measurements and the error bars represent the standard deviation. Both samples present a same elastic modulus value  $E_{IT} = 188 \pm 3$  GPa, obtained by considering a Poisson ratio  $\nu=0.34$  for both films (in agreement with the effective elastic constants reported in Table 4). The elastic modulus is found to be independent of the true penetration depth  $h_c$  in the 25 – 60 nm range. This behavior is also an evidence of a good indenter tip calibration since the elastic modulus is not supposed to depend on the penetration depth, at least for small penetration depths compared to the film thickness (~325 nm). The slight variation observed in the  $\alpha$ -Ta film for penetration depths lower than 25 nm is likely to be



due to surface roughness effect, which has been observed to be higher in this sample. This roughness effect would also explain the increase in the scattering of the data. Regarding the hardness, the  $\alpha$ -Ta film presents a constant hardness value,  $H=10.3 \pm 0.5$  GPa, over a penetration depth of more than 80 nm. The  $\beta$ -Ta film is found to exhibit a much higher hardness, slightly dependent on the penetration depth, with a peak value  $H=18.0 \pm 0.3$  GPa at  $h_c=35$  nm.

Figure 7b shows two typical nanoindentation curves obtained in both Ta films for the same maximum penetration depth of 50 nm. A larger elastic recovery is observed for the  $\beta$ -Ta film. One of the residual indent obtained in the  $\beta$ -Ta sample for a true penetration depth  $h_c=110$  nm (residual depth  $h_p=80$  nm) has been observed by AFM. The topography image is presented in 3D top view in Fig. 7c with the inset showing the cross-section profile taken along the black line across the indent. It must be noticed that, despite the very high value of the hardness in this sample, the residual indent presents a remarkable ductile behavior, since no cracks nor indent bowing-in effects are observed.

## IV. Discussion

### IV.1. Textured films

The combination of PLU and BLS experiments allows for an independent determination of  $C_{33}$  and  $C_{44}$  effective elastic constants. Considering the resulting effective hexagonal symmetry of the textured films (transversely isotropic medium), five independent effective elastic constants  $\langle C_{ij} \rangle$  have been calculated using SC averaging [65,66], and the values reported in Table 4. For  $C_{33}$ , a remarkable agreement between experimental values and calculations is

obtained for both phases:  $C_{33}^{\alpha-Ta} = 285 \pm 3$  GPa and  $\langle C_{33}^{\alpha-Ta} \rangle = 286$  GPa, and  $C_{33}^{\beta-Ta} = 310 \pm 3$  GPa and  $\langle C_{33}^{\beta-Ta} \rangle = 304$  GPa. While the experimental shear elastic constant of  $\alpha$ -Ta film ( $C_{44}^{\alpha-Ta} = 69 \pm 1$  GPa) fairly agrees with the calculated one ( $\langle C_{44}^{\alpha-Ta} \rangle = 64$  GPa), a significant softening (more than 25%) is observed for the out-of-plane shear elastic constant of the  $\beta$ -Ta film ( $C_{44}^{\beta-Ta} = 50 \pm 1$  GPa) compared to the calculated value ( $\langle C_{44}^{\beta-Ta} \rangle = 68$  GPa). As already discussed above, it has been previously shown that the  $C_{44}$  elastic constant of metastable sputter-deposited Mo-Si films was highly sensitive to structural disorder and metallic/insulator character, while the grain size had negligible influence, at least in ranges above 30 nm [69]. Since both  $\alpha$ -Ta and  $\beta$ -Ta films possess similar columnar morphology and grain sizes in the 30-50 nm range, the observed softening of  $C_{44}$  for  $\beta$ -Ta is surmised to be contributed to its higher structural disorder, inherently caused by interstitial-type point defects (e.g., Ar interstitials or cluster of self-interstitials).

A noticeable finding of the present work is the excellent agreement of the elastic Young's modulus obtained by nanoindentation technique ( $E_{IT} = 188$  GPa) and the value calculated using SC averaging, being in the 189-205 GPa range, if one considers the out-of-plane  $E_{\perp}$  component, see Table 4. These  $E$  values, together with the measured nanoindentation hardness ( $H = 10.3$  GPa for  $\alpha$ -Ta and  $H = 18.0$  GPa for  $\beta$ -Ta) are also in line with previous reports by Zhang *et al.* [34] and Shiri *et al.* [4].

#### IV.2. Virtual polycrystalline films

In this section, we extend our discussion on the elastic properties of tantalum allotropes to the case of weakly-textured or randomly oriented (*polycrystalline*) films, as this is a rather frequent case for sputter-deposition.

The independent determination of  $V_L$  and  $V_T$  data from PLU and BLS experiments also allows for the evaluation of the average sound velocity  $V_m$  in the polycrystalline film according to

$$\frac{3}{V_m^3} = \frac{1}{V_L^3} + \frac{2}{V_T^3} \quad (1)$$

In the Debye model, the characteristic temperature  $\theta_D$ , the so-called Debye temperature, is related to  $V_m$  using the following equation

$$\theta_D = \frac{\hbar}{k} \left( \frac{6\pi^2}{V_a} \right)^{1/3} V_m \quad (2)$$

where  $\hbar$  and  $k$  are the Planck's and Boltzmann's constants, respectively, and  $V_a$  is the atomic volume (see values reported in [Table 3](#)). Application of eq. (2) to the  $\alpha$ -Ta phase yields a Debye temperature  $\theta_D$  ( $\alpha$ -Ta) = 258 K, which is in remarkable agreement with the experimental value reported in the literature for bulk Ta ( $\theta_D^{\text{bulk Ta}}=250$  K) [70], and slightly lower than our theoretical estimation for  $\beta$ -Ta ( $\theta_D^{\beta\text{-Ta}}=266$  K). However, we find a lower experimental value  $\theta_D$  ( $\beta$ -Ta) = 221 K for the tetragonal structure, see [Table 5](#). This tendency involves a lower cohesion and also suggests a shift of the phonon density of states towards lower frequencies for  $\beta$ -Ta compared to  $\alpha$ -Ta. This result seems also correlated to the observed softening of the shear elastic constant  $C_{44}$ .

Using the two experimental effective elastic constants,  $C_{33}$  and  $C_{44}$ , we have calculated and reported in Table 5, the Young's modulus  $E$ , the shear modulus  $G$  ( $G=C_{44}$ ) and the bulk modulus  $B$ , considering an *isotropic* approximation and the following relations:

$$E = C_{33} - \frac{(C_{33}-2C_{44})^2}{C_{33}-C_{44}} \quad (3)$$

$$G = C_{44} \quad (4)$$

$$B = C_{33} - \frac{4}{3}C_{44} \quad (5)$$

For  $\alpha$ -Ta, the ratio  $G/E$  is  $\sim 0.373$ , which is very close to the value of  $3/8$  experimentally found for polycrystalline materials [71], and slightly higher than the theoretical value of  $0.367$  reported for bcc metals [72], providing us with a good confidence in our results. Pugh initially proposed a relationship based on the  $G/B$  ratio for polycrystalline metals and introduced a critical ratio  $(G/B)_{crit}$  allowing to define a scale going from ductile (at low  $G/B$  values) to brittle (at higher  $G/B$  values) [67]. This critical ratio depends on the crystalline structure of the material considered. This criterion has been later developed and quantified by others [73,74]. For bcc polycrystalline metals, the brittle-to-ductile transition, though not so well defined, is observed for an average value  $(G/B)_{crit} \sim 0.55$ . The  $G/B$  ratio being related to Poisson ratio, this limit can be equivalently thought off as a critical Poisson ratio [75]. Later, Pettifor introduced a criterion linking the brittle-to-ductile transition in polycrystalline cubic materials to the Cauchy pressure  $p$  ( $c_{12}-c_{66}$ ), ( $c_{13}-c_{55}$ ) and ( $c_{23}-c_{44}$ ), a parameter related to the angular character of bonds [76]. Based on his findings, positive Cauchy pressures correspond to a metallic character and to a ductile behavior of the material, while negative values involve a strong angular character of bonds, as observed in covalent bonding, and a brittle behavior. The ratio  $G/B$  reaches a value as lower as  $0.357$  and a high positive Cauchy pressure  $(c_{12}-c_{44}) = 78$  GPa is calculated for  $\alpha$ -Ta, that should result to a

good ductility behavior. For  $\beta$ -Ta, the ratio  $G/E \sim 0.356$  is slightly lower than  $3/8$ , whereas  $p = 67$ - $78$  GPa and Pugh's ratio  $G/B \sim 0.205$  predicting an even more ductile behavior. This is consistent with the AFM observation of the residual indents (see Fig. 7c) which were perfect reproductions of the Berkovich indenter shape, with no cracks or pile-up. These experiments demonstrate that the  $\alpha$ -Ta and  $\beta$ -Ta, despite their very high hardness, present a remarkable ductile behavior.

## V. Conclusions

The elastic and mechanical properties of  $\alpha$ -Ta and  $\beta$ -Ta were assessed both experimentally and from *ab initio* calculations. Measurements of two independent effective elastic constants,  $C_{33}$  and  $C_{44}$ , were performed by combining PLU and BLS techniques on single-phase, highly-textured and densely-packed Ta sputtered films. Both films exhibit similar  $C_{33}$  (285-310 GPa) and elastic Young's modulus ( $E_{IT} \sim 188$  GPa) values, in remarkable agreement with computed values. However, a substantial softening of the out-of-plane shear modulus was measured for the  $\beta$ -Ta film (50 vs. 69 GPa for  $\alpha$ -Ta), which together with its higher hardness (18 vs. 10.3 GPa for  $\alpha$ -Ta) yield  $H/E$  and  $G/B$  ratios of 0.10 and 0.20, respectively. Large positive Cauchy pressures, 70-80 GPa, are predicted for both Ta phases, confirming their metallic bonding character and ductile behavior.

The present findings reveal that, contrary to common beliefs, despite the fact that  $\beta$ -Ta allotropic phase being significantly harder than  $\alpha$ -Ta, it is not more brittle, but exhibits a ductile behavior, which makes it suitable as a protective coating for bio-medical applications where toughness and elastic compliance are of key importance.

**Acknowledgments**

The authors thank the Centre de Ressources Informatiques of the Université de Sciences et Technologies de Lille (CRI) for providing access to their computational facilities.

## References

- [1] S.M.M. Cardonne, P. Kumar, C.A.A. Michaluk, H.D.D. Schwartz, Tantalum and its alloys, *Int. J. Refract. Met. Hard Mater.* 13 (1995) 187–194. doi:10.1016/0263-4368(95)94023-R.
- [2] P. Catania, J.P. Doyle, J.J. Cuomo, Low resistivity body-centered cubic tantalum thin films as diffusion barriers between copper and silicon, *J. Vac. Sci. Technol. A.* 10 (1992) 3318–3321.
- [3] L. Gladczuk, A. Patel, C. Singh Paur, M. Sosnowski, Tantalum films for protective coatings of steel, *Thin Solid Films.* 467 (2004) 150–157.
- [4] S. Shiri, C. Zhang, A. Odeshi, Q. Yang, Growth and characterization of tantalum multilayer thin films on CoCrMo alloy for orthopedic implant applications, *Thin Solid Films.* 645 (2018) 405–408. doi:10.1016/j.tsf.2017.11.017.
- [5] L.L. Liu, J. Xu, X. Lu, P. Munroe, Z.-H. Xie, Electrochemical Corrosion Behavior of Nanocrystalline  $\beta$ -Ta Coating for Biomedical Applications, *ACS Biomater. Sci. Eng.* 2 (2016) 579–594.
- [6] V.-H. Pham, S.-H. Lee, Y. Li, H.-E. Kim, K.-H. Shin, Y.-H. Koh, Utility of tantalum (Ta) coating to improve surface hardness in vitro bioactivity and biocompatibility of Co–Cr, *Thin Solid Films.* 536 (2013) 269–274.
- [7] X. Li, L. Wang, X. Yu, Y. Feng, C. Wang, K. Yang, D. Su, Tantalum coating on porous Ti6Al4V scaffold using chemical vapor deposition and preliminary biological evaluation, *Mater. Sci. Eng. C.* 33 (2013) 2987–2994. doi:10.1016/J.MSEC.2013.03.027.
- [8] H. Moreira, A. Costa-Barbosa, S.M. Marques, P. Sampaio, S. Carvalho, Evaluation of cell activation promoted by tantalum and tantalum oxide coatings deposited by reactive DC magnetron sputtering, *Surf. Coatings Technol.* 330 (2017) 260–269. doi:10.1016/J.SURFCOAT.2017.10.019.
- [9] A. Bendavid, H. Cao, A.C. Hee, P.J. Martin, Y. Zhao, S.S. Jamali, Cytocompatible tantalum films on Ti6Al4V substrate by filtered cathodic vacuum arc deposition, *Bioelectrochemistry.* 122 (2018) 32–39. doi:10.1016/j.bioelechem.2018.02.006.
- [10] R.B. Marcus, S. Quigley, Formation of f.c.c., b.c.c. and  $\beta$ -tantalum films by evaporation, *Thin Solid Films.* 2 (1968) 467–477. doi:10.1016/0040-6090(68)90060-6.
- [11] M.T. Janish, W.M. Mook, C.B. Carter, Nucleation of fcc Ta when heating thin films, *Scr. Mater.* 96 (2015) 21–24. doi:10.1016/J.SCRIPTAMAT.2014.10.010.
- [12] S. Shiri, A. Odeshi, N. Chen, R. Feng, R. Sutarto, Q. Yang, FCC tantalum thin films deposited by magnetron sputtering, *Surf. Coatings Technol.* 358 (2019) 942–946.

doi:10.1016/j.surfcoat.2018.12.015.

- [13] D.W. Matson, E.D. McClanahan, J.P. Rice, S.L. Lee, D. Windover, Effect of sputtering parameters on Ta coatings for gun bore applications, *Surf. Coatings Technol.* 133–134 (2000) 411–416.
- [14] S. Myers, J. Lin, R.M. Souza, W.D. Sproul, J.J. Moore, The  $\beta$  to  $\alpha$  phase transition of tantalum coatings deposited by modulated pulsed power magnetron sputtering, *Surf. Coatings Technol.* 214 (2013) 38–45.
- [15] J.J. Colin, G. Abadias, A. Michel, C. Jaouen, On the origin of the metastable  $\beta$ -Ta phase stabilization in tantalum sputtered thin films, *Acta Mater.* 126 (2017) 481–493.  
doi:10.1016/j.actamat.2016.12.030.
- [16] L.G. Feinstein, R.D. Huttemann, Annealing and phase stability of tantalum films sputtered in Ar-O<sub>2</sub>, *Thin Solid Films.* 20 (1974) 103–114.
- [17] L.A. Clevenger, A. Mutscheller, J.M.E. Harper, C. Cabral, K. Barmak, The relationship between deposition conditions, the beta to alpha phase transformation, and stress relaxation in tantalum thin films, *J. Appl. Phys.* 72 (1992) 4918–4924.
- [18] R. Knepper, S.P. Baker, Coefficient of thermal expansion and biaxial elastic modulus of  $\beta$  phase tantalum thin films, *Appl. Phys. Lett.* 90 (2007) 181908.
- [19] S. Sato, Nucleation properties of magnetron-sputtered tantalum, *Thin Solid Films.* 94 (1982) 321–329.
- [20] D. Bernoulli, U. Müller, M. Schwarzenberger, R. Hauert, R. Spolenak, Magnetron sputter deposited tantalum and tantalum nitride thin films: An analysis of phase, hardness and composition, *Thin Solid Films.* 548 (2013) 157–161.
- [21] D.W. Face, D.E. Prober, Nucleation of body-centered-cubic tantalum films with a thin niobium underlayer, *J. Vac. Sci. Technol. A.* 5 (1987) 3408–3412.
- [22] A. Schauer, M. Roschy, R.F. sputtered  $\beta$ -tantalum and b.c.c. tantalum films, *Thin Solid Films.* 12 (1972) 313–317. doi:10.1016/0040-6090(72)90095-8.
- [23] S.. Lee, D. Windover, T.-M. Lu, M. Audino, In situ phase evolution study in magnetron sputtered tantalum thin films, *Thin Solid Films.* 420 (2002) 287–294.
- [24] H. Ren, M. Sosnowski, Tantalum thin films deposited by ion assisted magnetron sputtering, *Thin Solid Films.* 516 (2008) 1898–1905.
- [25] K. Ino, T. Shinohara, T. Ushiki, T. Ohmi, Ion energy, ion flux, and ion species effects on crystallographic and electrical properties of sputter-deposited Ta thin films, *J. Vac. Sci. Technol. A.* 15 (1997) 2627–237.
- [26] P. Catania, R.A. Roy, J.J. Cuomo, Phase formation and microstructure changes in tantalum thin films induced by bias sputtering, *J. Appl. Phys.* 74 (1993) 1008–1014.



- [27] J. Alami, P. Eklund, J.M. Andersson, M. Lattemann, E. Wallin, J. Bohlmark, P. Persson, U. Helmersson, Phase tailoring of Ta thin films by highly ionized pulsed magnetron sputtering, *Thin Solid Films*. 515 (2007) 3434–3438.
- [28] A.A. Navid, A.M. Hodge, Nanostructured alpha and beta tantalum formation—Relationship between plasma parameters and microstructure, *Mater. Sci. Eng. A*. 536 (2012) 49–56.
- [29] E.A.I. Ellis, M. Chmielus, S.P. Baker, Effect of sputter pressure on Ta thin films: Beta phase formation, texture, and stresses, *Acta Mater.* 150 (2018) 317–326. doi:10.1016/j.actamat.2018.02.050.
- [30] M.H. Read, C. Altman, A new structure in tantalum thin films, *Appl. Phys. Lett.* 7 (1965) 51.
- [31] P.N. Baker, Preparation and properties of tantalum thin films, *Thin Solid Films*. 14 (1972) 3–25.
- [32] N.N. Kovaleva, D. Chvostova, A. V. Bagdinov, M.G. Petrova, E.I. Demikhov, F.A. Pudonin, A. Dejneka, Interplay of electron correlations and localization in disordered  $\beta$ -tantalum films: Evidence from dc transport and spectroscopic ellipsometry study, *Appl. Phys. Lett.* 106 (2015) 51907. doi:10.1063/1.4907862.
- [33] M. Zhang, B. Yang, J. Chu, T.G. Nieh, Hardness enhancement in nanocrystalline tantalum thin films, *Scr. Mater.* 54 (2006) 1227–1230.
- [34] M. Zhang, Y.F. Zhang, P.D. Rack, M.K. Miller, T.G. Nieh, Nanocrystalline tetragonal tantalum thin films, *Scr. Mater.* 57 (2007) 1032–1035.
- [35] S. Frank, P.A. Gruber, U.A. Handge, R. Spolenak, In situ studies on the cohesive properties of  $\alpha$ - and  $\beta$ -Ta layers on polyimide substrates, *Acta Mater.* 59 (2011) 5881–5892.
- [36] K.W. Katahara, M.H. Manghnani, E.S. Fisher, Pressure derivatives of the elastic moduli of niobium and tantalum, *J. Appl. Phys.* 47 (1976) 434–439. doi:10.1063/1.322666.
- [37] P. Söderlind, J.A. Moriarty, First-principles theory of Ta up to 10 Mbar pressure: Structural and mechanical properties, *Phys. Rev. B*. 57 (1998) 10340–10350. doi:10.1103/PhysRevB.57.10340.
- [38] A. Strachan, T. Çağın, O. Gülseren, S. Mukherjee, R.E. Cohen, W.A. Goddard III, First principles force field for metallic tantalum, *Model. Simul. Mater. Sci. Eng.* 12 (2004) S445–S459. doi:10.1088/0965-0393/12/4/S10.
- [39] C. Bercegeay, S. Bernard, First-principles equations of state and elastic properties of seven metals, *Phys. Rev. B - Condens. Matter Mater. Phys.* 72 (2005) 1–9. doi:10.1103/PhysRevB.72.214101.
- [40] G. Kresse, J. Furthmüller, Efficient iterative schemes for ab initio total-energy calculations using a plane-wave basis set, *Phys. Rev. B*. 54 (1996) 11169–11186.

- [41] G. Kresse, From ultrasoft pseudopotentials to the projector augmented-wave method, *Phys. Rev. B.* 59 (1999) 1758–1775.
- [42] J.P. Perdew, K. Burke, M. Ernzerhof, Generalized Gradient Approximation Made Simple, *Phys. Rev. Lett.* 77 (1996) 3865–3868.
- [43] A. Arakcheeva, G. Chapuis, V. Grinevitch, The self-hosting structure of  $\beta$ -Ta, *Acta Crystallogr. Sect. B Struct. Crystallogr. Cryst. Chem.* 58 (2002) 1–7.
- [44] S.K.R. Patil, S. V. Khare, B.R. Tuttle, J.K. Bording, S. Kodambaka, Mechanical stability of possible structures of PtN investigated using first-principles calculations, *Phys. Rev. B.* 73 (2006) 104118.
- [45] A. Djied, H. Khachai, T. Seddik, R. Khenata, A. Bouhemadou, N. Guechi, G. Murtaza, S. Bin-Omran, Z.A. Alahmed, M. Ameri, Structural phase transition, mechanical and optoelectronic properties of the tetragonal NaZnP: Ab-initio study, *Comput. Mater. Sci.* 84 (2013) 396–403.
- [46] F.D. Murnaghan, The Compressibility of Media under Extreme Pressures, *Proc. Natl. Acad. Sci. U. S. A.* 30 (1944) 244–247.
- [47] J.J. Colin, Y. Diot, P. Guerin, B. Lamongie, F. Berneau, A. Michel, C. Jaouen, G. Abadias, A load-lock compatible system for in situ electrical resistivity measurements during thin film growth, *Rev. Sci. Instrum.* 87 (2016) 23902.
- [48] A. Fillon, G. Abadias, A. Michel, C. Jaouen, Stress and microstructure evolution during growth of magnetron-sputtered low-mobility metal films : Influence of the nucleation conditions, *Thin Solid Films.* 519 (2010) 1655–1661. doi:10.1016/j.tsf.2010.07.091.
- [49] I. Horcas, R. Fernández, J.M. Gómez-Rodríguez, J. Colchero, J. Gómez-Herrero, A.M. Baro, WSXM: A software for scanning probe microscopy and a tool for nanotechnology, *Rev. Sci. Instrum.* 78 (2007) 13705. doi:10.1063/1.2432410.
- [50] G. Abadias, P. Djemia, L. Belliard, Alloying effects on the structure and elastic properties of hard coatings based on ternary transition metal (M=Ti, Zr or Ta) nitrides, *Surf. Coatings Technol.* 257 (2014) 129–137.
- [51] F. Faëse, D. Poinot-Cherroret, S. Chatel, L. Becerra, F. Challali, P. Djemia, L. Belliard, Mechanical properties of elementary layers involved in a multilayer optical stack by photon-acoustic phonon interaction approaches, *J. Appl. Phys.* 124 (2018) 125307.
- [52] J. Woigard, J.C. Dargenton, An alternative method for penetration depth determination in nanoindentation measurements, *J. Mater. Res.* 12 (1997) 2455–2458.
- [53] W.C. Oliver, G.M. Pharr, Measurement of hardness and elastic modulus by instrumented indentation: Advances in understanding and refinements to methodology, *J. Mater. Res.* 19 (2004) 3–20.
- [54] C. Thomsen, J. Strait, Z. Vardeny, H.J. Maris, J. Tauc, J.J. Hauser, Coherent Phonon Generation and Detection by Picosecond Light Pulses, *Phys. Rev. Lett.* 53 (1984) 989–992.

- [55] C. Thomsen, H.T. Grahn, H.J. Maris, J. Tauc, Surface generation and detection of phonons by picosecond light pulses, *Phys. Rev. B.* 34 (1986) 4129–4138. doi:10.1103/PhysRevB.34.4129.
- [56] A. Fillon, C. Jaouen, A. Michel, G. Abadias, C. Tromas, L. Belliard, B. Perrin, P. Djemia, Lattice instability and elastic response of metastable Mo<sub>1-x</sub>Si<sub>x</sub> thin films, *Phys. Rev. B - Condens. Matter Mater. Phys.* 88 (2013) 174104. doi:10.1103/PhysRevB.88.174104.
- [57] L. Belliard, A. Huynh, B. Perrin, A. Michel, G. Abadias, C. Jaouen, Elastic properties and phonon generation in Mo/Si superlattices, *Phys. Rev. B - Condens. Matter Mater. Phys.* 80 (2009) 155424. doi:10.1103/PhysRevB.80.155424.
- [58] F. Nizzoli, J.R. Sandercock, Surface Brillouin scattering from phonons, in: G.K. Horton, A.A. Maradudin (Eds.), *Dyn. Prop. Solids*, North Holland, Amsterdam, 1990: pp. 281–335.
- [59] P. Djemia, F. Ganot, P. Moch, V. Branger, P. Goudeau, Brillouin scattering investigation of elastic properties of Cu–Mo solid solution thin films, *J. Appl. Phys.* 90 (2001) 756–762. doi:10.1063/1.1378331.
- [60] A. Kueny, M. Grimsditch, Surface waves in a layered material, *Phys. Rev. B.* 26 (1982) 4699–4702. doi:10.1103/PhysRevB.26.4699.
- [61] L.G. Parratt, Surface Studies of Solids by Total Reflection of X-Rays, *Phys. Rev.* 95 (1954) 359–369.
- [62] G.K. Williamson, W.H. Hall, X-ray line broadening from fcc aluminium and wolfram, *Acta Metall.* 1 (1953) 22–31.
- [63] J.P. Singh, T. Karabacak, T.M. Lu, G.C. Wang, Nanoridge domains in  $\alpha$ -phase W films, *Surf. Sci.* 538 (2003) L483–L487.
- [64] F.H. Featherston, The elastic constants of Tantalum and Molybdenum, *Phys. Rev.* 130 (1963) 1324–1333.
- [65] R. Brenner, O. Castelnau, L. Badea, Mechanical field fluctuations in polycrystals estimated by homogenization techniques, *Proc. R. Soc. London. Ser. A Math. Phys. Eng. Sci.* 460 (2004) 3589–3612. doi:10.1098/rspa.2004.1278.
- [66] D. Faurie, P. Djemia, E. Le Bourhis, P.-O. Renault, Y. Roussigné, S.M. Chérif, R. Brenner, O. Castelnau, G. Patriarche, P. Goudeau, Elastic anisotropy of polycrystalline Au films: Modeling and respective contributions of X-ray diffraction, nanoindentation and Brillouin light scattering, *Acta Mater.* 58 (2010) 4998–5008. doi:10.1016/j.actamat.2010.05.034.
- [67] S.F. Pugh, Relations between the elastic moduli and the plastic properties of polycrystalline pure metals, *Philos. Mag.* 45 (1954) 823–843.
- [68] H.T. Chen, M.F. Yan, Influence of interstitial distribution on the elastic and electronic properties of  $\epsilon$ -Fe<sub>6</sub>NxCy phase by first-principles calculations, *Phys. Lett. A.* 378 (2014) 270–275. doi:10.1016/J.PHYSLETA.2013.11.008.

- [69] P. Djemia, A. Fillon, G. Abadias, A. Michel, C. Jaouen, Elastic properties of metastable Mo<sub>1-x</sub>Si<sub>x</sub> alloy thin films: A Brillouin light scattering study, *Surf. Coatings Technol.* 206 (2011) 1824–1829. doi:10.1016/j.surfcoat.2011.08.003.
- [70] T. Mamiya, K. Nomura, Y. Masuda, Superconductivity of Tantalum-Rhenium Alloys, *J. Phys. Soc. Japan.* 28 (1970) 380–389. doi:10.1143/JPSJ.28.380.
- [71] C. Zwikker, *Physical Properties of Solid Materials*, Pergamon Press, London, 1954.
- [72] H.M. Ledbetter, Ratio of the shear and Young's Moduli for polycrystalline metallic elements, *Mater. Sci. Eng.* 27 (1977) 133–135. doi:10.1016/0025-5416(77)90165-3.
- [73] J.R. Rice, R. Thomson, Ductile versus brittle behaviour of crystals, *Philos. Mag.* 29 (1974) 73–97.
- [74] A.H. Cottrell, *Advances in Physical Metallurgy*, in: J.A. Charles, G.C. Smith (Eds.), *Institute of Metals*, London, 1990: pp. 181–187.
- [75] Z.Q. Liu, W.H. Wang, M.Q. Jiang, Z.F. Zhang, Intrinsic factor controlling the deformation and ductile-to-brittle transition of metallic glasses, *Philos. Mag. Lett.* 94 (2014) 658–668. doi:10.1080/09500839.2014.955548.
- [76] D.G. Pettifor, Theoretical predictions of structure and related properties of intermetallics, *Mater. Sci. Technol.* 8 (1992) 345–349. doi:10.1179/mst.1992.8.4.345.

**Table 1** : Wyckoff positions of Ta atoms in the tetragonal cell of  $\beta$ -Ta phase, as compared to those reported by Arakcheeva *et al.* [43]. The calculated atomic volume is  $V_a = 18.2 \text{ \AA}^3$  for  $\alpha$ -Ta and  $V_a = 18.7 \text{ \AA}^3$  for  $\beta$ -Ta

Wyckoff positions	x	y	z		-
2c	0.500	0.000	0.245		Present
	0.500	0.000	0.228		[43]
4e(1)	0.105	0.395	0.256		Present
	0.103	0.397	0.235		[43]
4e(2)	0.819	0.319	0.002		Present
	0.814	0.314	0.003		[43]
4e(3)	0.819	0.319	0.500		Present
	0.820	0.320	0.491		[43]
8f(1)	0.761	0.067	0.246		Present
	0.760	0.068	0.235		[43]
8f(2)	0.035	0.129	0.254		Present
	0.035	0.127	0.255		[43]

**Table 2:** Results of DFT calculations for  $\alpha$ -Ta and  $\beta$ -Ta phases: lattice parameter, zero-temperature bulk modulus  $B_0$  and single-crystal elastic constants  $c_{ij}$ . Values in bold correspond to the present work.

	$\alpha$ -Ta	$\beta$ -Ta	Method (package)	References
Space group	$Im\bar{3}m$	$P\bar{4}2_1m$		
Lattice parameter $a$ (nm)	<b>0.332</b> 0.330 0.332	<b>1.025</b>  1.021	PP-GGA (VASP) PP-GGA (ABINIT) LAPW-GGA <i>exp</i>	present work [39] [38] [43]
Lattice parameter $c$ (nm)	/	<b>0.534</b> 0.531	PP-GGA (VASP) <i>exp</i>	present work [43]
$c_{11}$ (GPa)	<b>260</b> 259 245 281 266 266	<b>295</b>	PP-GGA (VASP) PP-GGA (ABINIT) LAPW-GGA LMTO-GGA <i>exp</i> <i>exp</i>	present work [39] [38] [37] [64] [36]
$c_{12}$ (GPa)	<b>157</b> 169 160 163 158 161	<b>136</b>	PP-GGA (VASP) PP-GGA (ABINIT) LAPW-GGA LMTO-GGA <i>exp</i> <i>exp</i>	present work [39] [38] [37] [64] [36]
$c_{13}$ (GPa)	= $c_{12}$	<b>146</b>		
$c_{33}$ (GPa)	= $c_{11}$	<b>304</b>		
$c_{44}$ (GPa)	<b>79</b> 68 68 93 87 83	<b>68</b>	PP-GGA (VASP) PP-GGA (ABINIT) LAPW-GGA LMTO-GGA <i>exp</i> <i>exp</i>	present work [39] [38] [37] [64] [36]
$c_{66}$ (GPa)	= $c_{44}$	<b>69</b>		
$B_0$ (GPa)	<b>191</b> 199 188 203 194 196	<b>194</b>	PP-GGA (VASP) PP-GGA (ABINIT) LAPW-GGA LMTO-GGA <i>exp</i> <i>exp</i>	present work [39] [38] [37] [64] [36]

**Table 3:** Properties of  $\alpha$ -Ta and  $\beta$ -Ta films determined experimentally.

	$\alpha$ -Ta		$\beta$ -Ta	
Film thickness (nm)	107	320	109	327
Mass density ( $\text{g.cm}^{-3}$ )	17.1	17.1	16.6	16.8
$V_a$ ( $\text{\AA}^3$ )	17.6	17.6	18.1	17.9
Texture	(110)	(110)	(002)	(002)
$V_L$ (km/s)	3.90	4.09	4.34	4.35
$V_T$ (km/s)	/	2.01	/	1.73
$C_{44}$ (GPa)	/	$69 \pm 1$	/	$50 \pm 1$
$C_{33}$ (GPa)	$260 \pm 3$	$285 \pm 3$	$309 \pm 3$	$310 \pm 3$
Hardness (GPa)	/	$10.3 \pm 0.3$	/	$18.0 \pm 0.3$
Elastic modulus, $E_{IT}$ (GPa)	/	$188 \pm 3$	/	$188 \pm 3$
Electrical resistivity ( $\mu\Omega.\text{cm}$ )	21.5	20.9	170.0	178.6

**Table 4:** Self-consistent average effective elastic constants  $\langle C_{ij} \rangle$  and elastic Young's modulus  $E$  and shear modulus  $G$  (in GPa) calculated for the experimentally observed crystallographic texture of tantalum films.

	$\langle C_{11} \rangle$	$\langle C_{12} \rangle$	$\langle C_{13} \rangle$	$\langle C_{33} \rangle$	$\langle C_{44} \rangle$ $G_{xz}=G_{yz}$	$\langle C_{66} \rangle$ $G_{xy}$	$E_{\perp}$ $E_z$	$E_{\parallel}$ $E_x=E_y$
$\alpha$ -Ta <110>	283	147	144	286	64	68	189	184
$\beta$ -Ta <001>	290	141	146	304	68	75	205	197



**Table 5:** Effective elastic moduli ( $B$ ,  $G$  and  $E$ ) and Debye temperature  $\theta_D$  of virtual *polycrystalline*  $\alpha$ -Ta and  $\beta$ -Ta films. “*exp*” refers to values calculated from experimental data considering isotropic approximation. For comparison, values calculated for a polycrystalline aggregate using computed  $\langle C_{ij} \rangle$  values of Table 4 are also given (noted as “*calc*”).

	$B$ (GPa)	$G$ (GPa)	$E$ (GPa)	$G/E$	$G/B$	$H/E_{IT}$ (°)	$\theta_D$ (K)
$\alpha$ -Ta <i>exp</i>	193±3	69±1	185±3	0.373	0.357	0.05	258
$\alpha$ -Ta <i>calc</i>	191	67	179	0.374	0.350	/	250 <sup>b</sup>
$\beta$ -Ta <i>exp</i>	243±3	50±1	140±3	0.356	0.205	0.10	221
$\beta$ -Ta <i>calc</i>	194	72	192	0.375	0.371	/	266 <sup>c</sup>

a) calculated from nanoindentation tests

b) from Ref. [70]

c) this work, calculated from DFT

### Figure captions

**Figure 1:**  $\beta$ -Ta tetragonal cell of  $P\bar{4}2_1m$  structure with Wyckoff positions c, e and f of Ta atoms, see Table 1.

**Figure 2:** XRR scans of  $\beta$ -Ta and  $\alpha$ -Ta films deposited on  $\alpha$ -Si and c-Mo buffer layer, respectively. Solid lines correspond to best-fit to experimental data (symbols).

**Figure 3:** XRD patterns of Ta films deposited on a)  $\alpha$ -Si and b) c-Mo buffer layers. The angular region around the 001 and 003 XRD lines of  $\beta$ -Ta film is shown in c).

**Figure 4:**  $1 \times 1 \mu\text{m}^2$  surface topography AFM images of a)  $\beta$ -Ta and b)  $\alpha$ -Ta films. Plan-view SEM micrographs are shown in the inset.

**Figure 5:** Transient reflectivity change measured by PLU on (a)  $\beta$ -Ta (327 nm) and (b)  $\alpha$ -Ta (319 nm) polycrystalline films. At least two echoes are indicated by the arrows from which the TOF is measured.

**Figure 6:** BLS spectra of (a)  $\beta$ -Ta (327 nm) and (b)  $\alpha$ -Ta (319 nm) polycrystalline films. The angle of incidence is  $70^\circ$ ,  $R$  denotes the Rayleigh surface wave and  $S_1$  the first Sezawa standing wave.

**Figure 7:** a) Depth-dependence of hardness (filled symbols) and elastic modulus (open symbols) of  $\alpha$ -Ta and  $\beta$ -Ta films extracted from nanoindentation tests. b) Representative nanoindentation curves of  $\alpha$ -Ta and  $\beta$ -Ta films (maximum penetration depth of  $h_c=50$  nm). c) AFM image around residual indent ( $h_c=110$  nm) of the  $\beta$ -Ta film, and corresponding height profile.

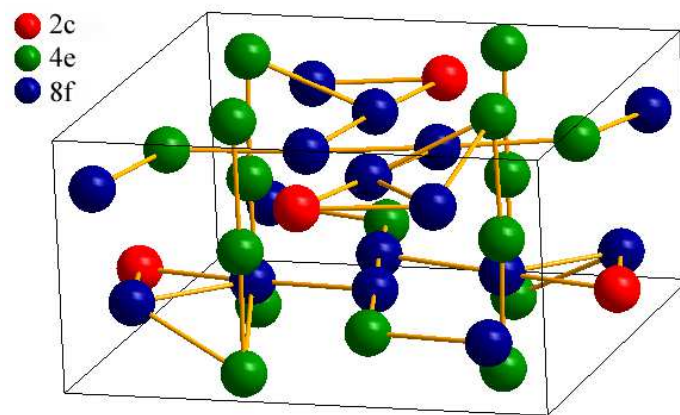


Figure 1

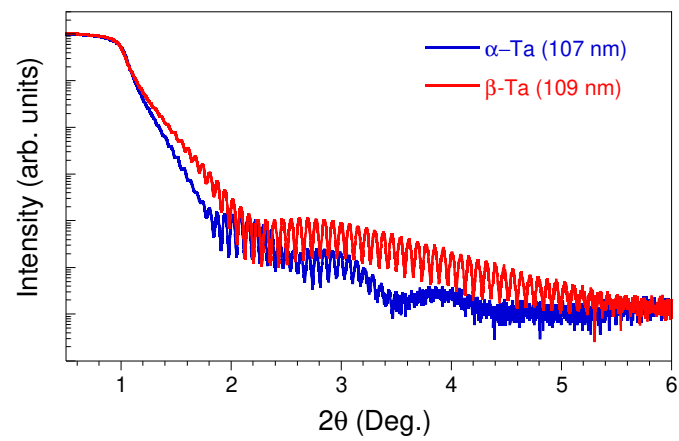


Figure 2

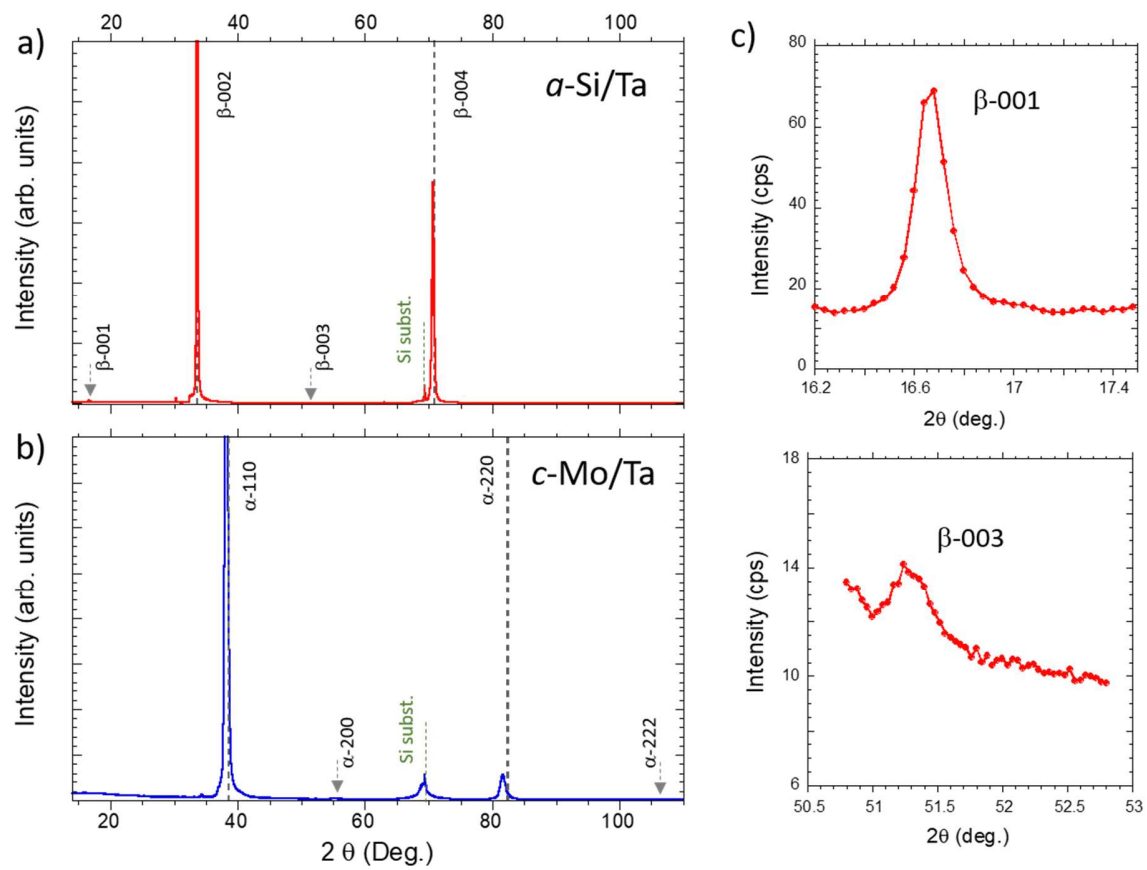


Figure 3

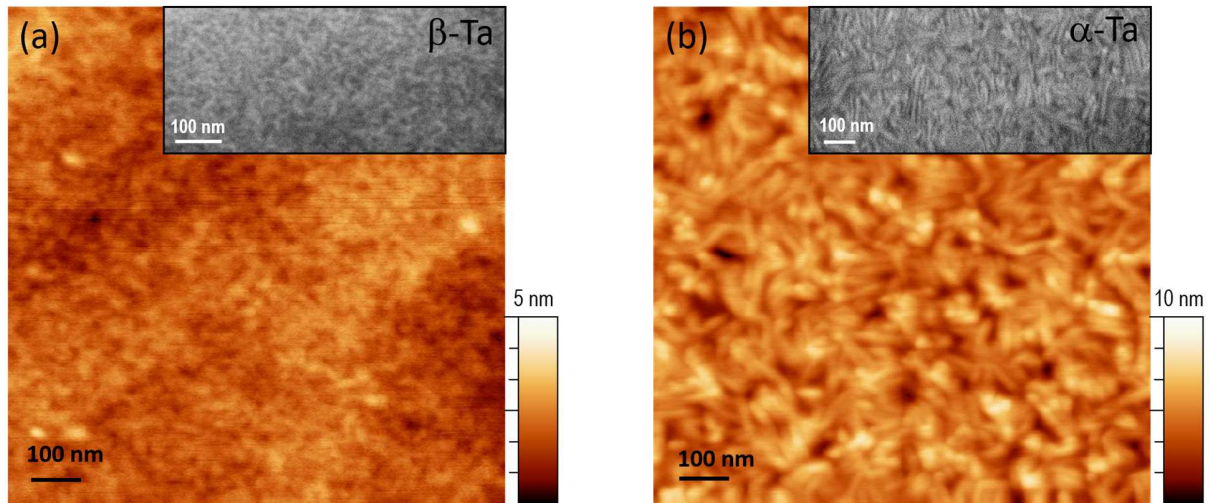


Figure 4

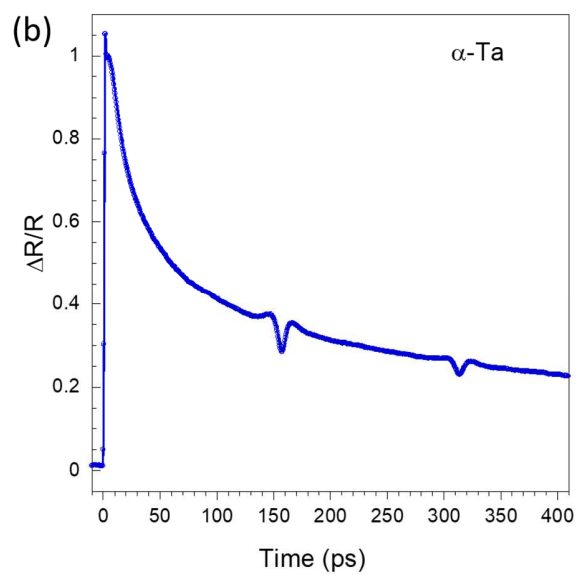
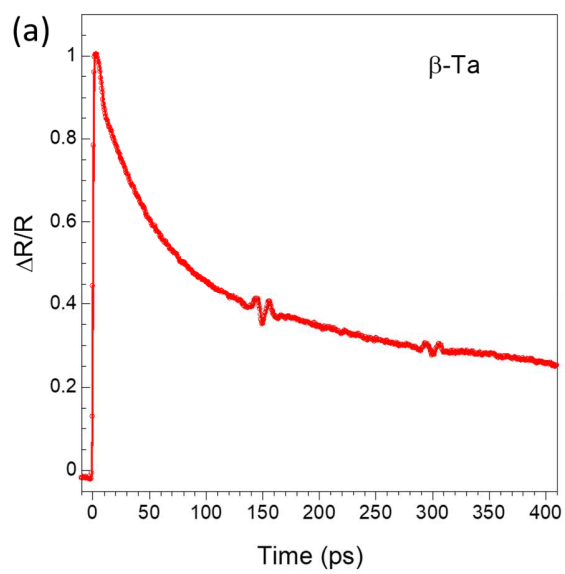


Figure 5

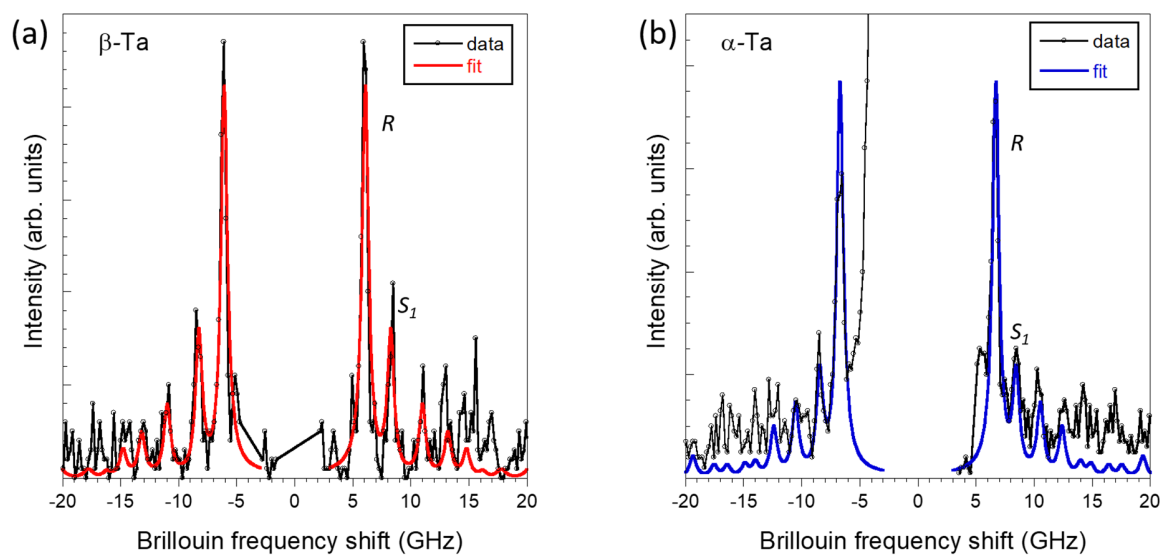


Figure 6



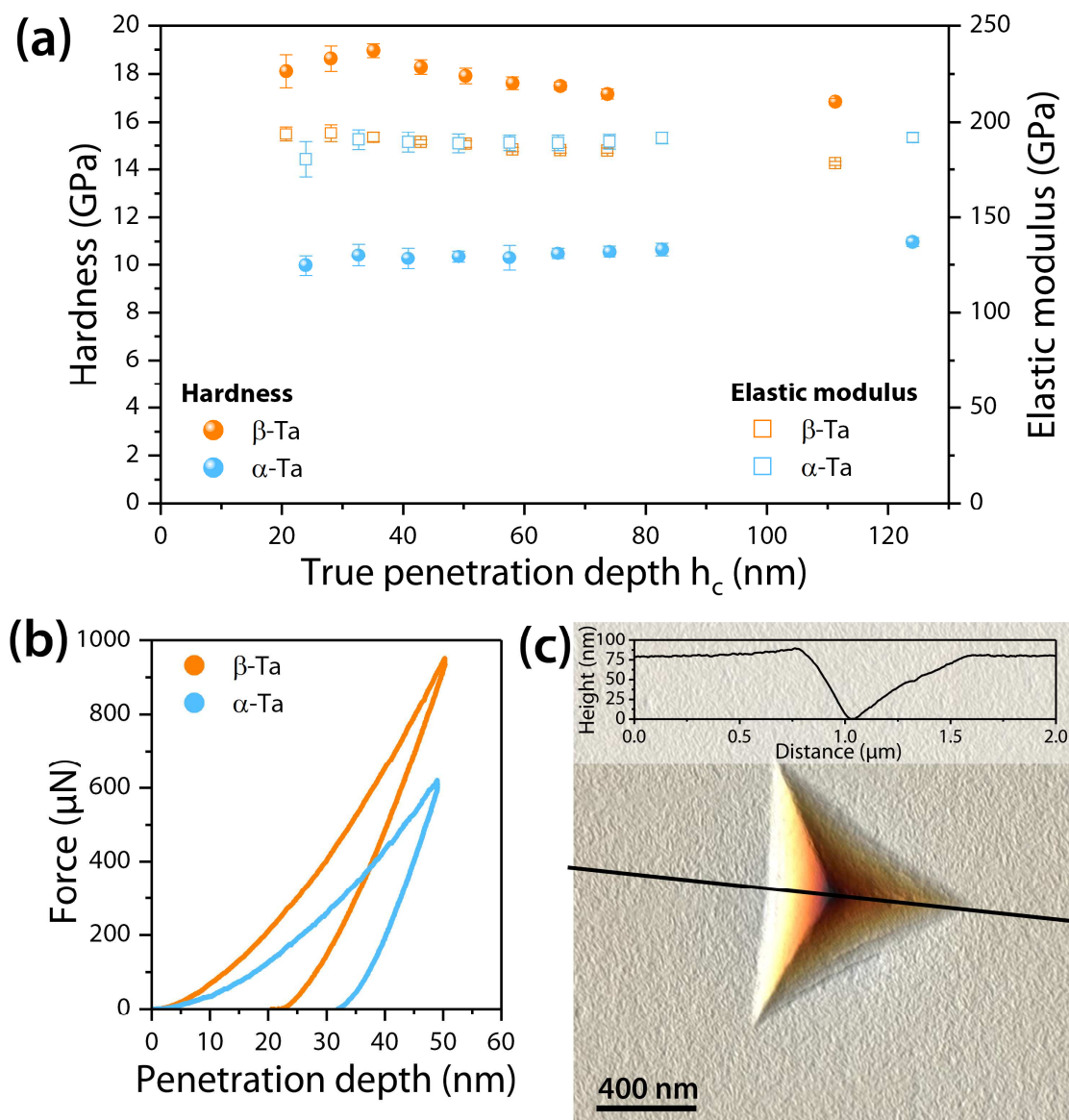


Figure 7